TECHNISCHE UNIVERSITÄT DRESDEN

INSTITUTE OF NUCLEAR AND PARTICLE PHYSICS

Sensitivity studies for the observation of electroweak diphoton+jets production at the LHC

Bachelor-Arbeit
zur Erlangung des Hochschulgrades
Bachelor of Science
im Bachelor-Studiengang Physik

vorgelegt von

Florens Förster
geboren am 08.11.2001 in Zschopau

Institut für Kern- und Teilchenphysik
Fakultät Physik
Bereich Mathematik und Naturwissenschaften
Technische Universität Dresden

2022

Eingereicht am 12. September 2022

1. Gutachter: Dr. Frank Siegert
2. Gutachter: Prof. Dr. Dominik Stöckinger

Summary

Abstract
English:
Processes involving the scattering or fusion of the weak vector bosons are extremely interesting for confirming the Standard Model of particle physics or discovering effects beyond it. In this thesis the fusion of vector bosons to photons is investigated using the production of two photons and two jets in scattering processes at the Large Hadron Collider. Criteria are to be found which will make a measurement sensitive to vector boson fusion. By simulating the corresponding processes, such criteria are optimized in this thesis, which ultimately leads to an expected statistical significance of the observation of electroweak production of two photons of around 33σ. Such a measurement is therefore sensitive to the desired process. Furthermore, the influences of systematic uncertainties and different simulations are discussed.

Abstract
Deutsch:
Prozesse, die die Streuung oder Fusion der schwachen Vektorbosonen enthalten, sind ungemein interessant für die Bestätigung des Standardmodells der Teilchenphysik oder die Entdeckung von Effekten darüber hinaus. In dieser Arbeit wird die Fusion von Vektorbosonen zu Photonen anhand der Produktion von zwei Photonen und zwei Jets in Streuprozessen am Large Hadron Collider untersucht. Dabei sollen Kriterien gefunden werden, mit denen sich eine auf die Vektorbosonenfusion sensible Messung durchführen lässt. Durch Simulation der entsprechenden Prozesse werden solche Kriterien in dieser Arbeit optimiert, was letztendlich zu einer erwarteten statistischen Signifikanz der Beobachtung elektroschwacher Produktion von zwei Photonen von rund 33σ führt. Damit ist eine solche Messung sensibel auf den gewünschten Prozess. Es werden weiterhin die Einflüsse systematischer Unsicherheiten und verschiedener Simulationen diskutiert.

Contents

1 Introduction

One of the main goals of modern particle physics is the examination of the Standard Model using particle colliders in which all kinds of processes occur. In particular, Vector Boson Scattering (VBS) and Vector Boson Fusion (VBF), meaning the self-interaction of the weak vector bosons, is especially interesting, since these rare processes with the high-mass participants might provide a further understanding of the Standard Model electroweak symmetry breaking or even indicate effects beyond the Standard Model. Because of their rarity and the high masses of the W and Z Bosons, the observation of those processes needs high luminosity particle accelerators and high energy collisions. For this thesis, that will be the Large Hadron Collider in Run 2 with $\sqrt{s} = 13$ TeV and an integrated luminosity of $L = 139/\text{fb}$ at the ATLAS detector. Out of all the possible processes including vector bosons, the focus for this study will be on the quartic $W^+W^-\gamma\gamma$ Vertex (see fig. 1.1) which, in the Standard Model, arises from the the $SU(2)_L$ gauge invariance and the electroweak unification.

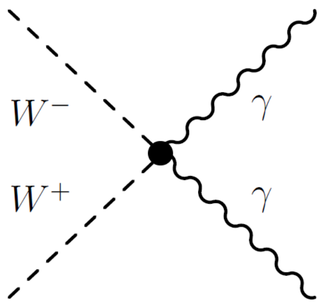

Figure 1.1: Qartic $W^+W^-\gamma\gamma$ vertex

To study this vertex, the production of two photons within proton-proton collisions will be simulated and the resulting events will be analyzed to gain information about the identification of this electroweak production process.

2 Theoretical Foundation

2.1 Diphoton Production

The process including the $W^+W^-\gamma\gamma$ vertex from proton-proton collisions is in total a $2 \rightarrow 4$ process from 2 partons to 2 photons and 2 jets. This outcome can achieved through many processes, most of them not containing any self interaction of vector bosons at all. For now, only leading order processes are considered, which means that exactly 4 vertices are to be found for all kinds of processes. They can be divided into electroweak (EW) processes, where all 4 vertices are electroweak, and the QCD-processes, where the interactions other than the production of the two photons are strong and described by quantum chromodynamics (QCD). The main target of this thesis is the extraction of the electroweak processes containing the quartic vertex fig. 1.1 from the QCD-background. Representative Feynman diagrams for both processes are given below (fig. 2.1 and fig. 2.2).

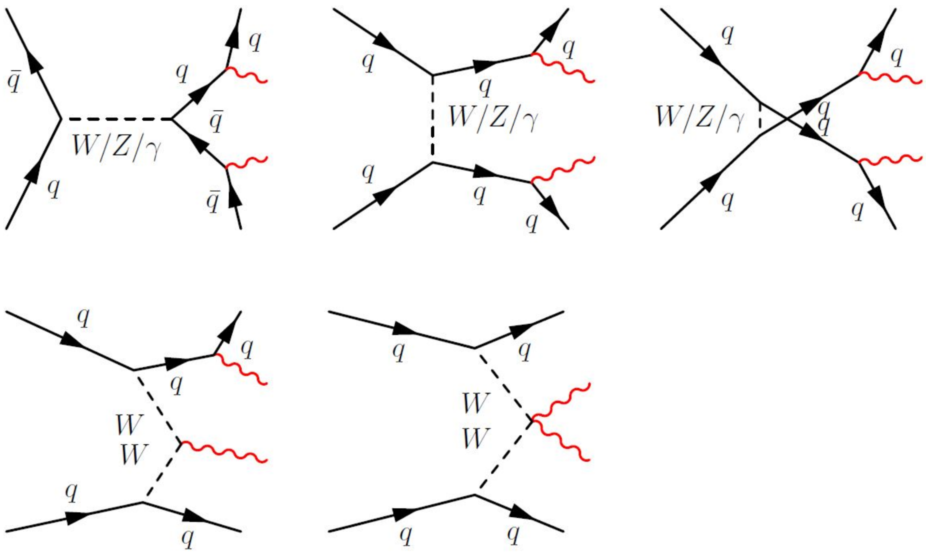

Figure 2.1: Representative Feynman diagrams for the electroweak production of two photons in proton-proton collisions in leading order. Photons are shown in red. The q represents any quarks or quark combination for which those processes can exist.

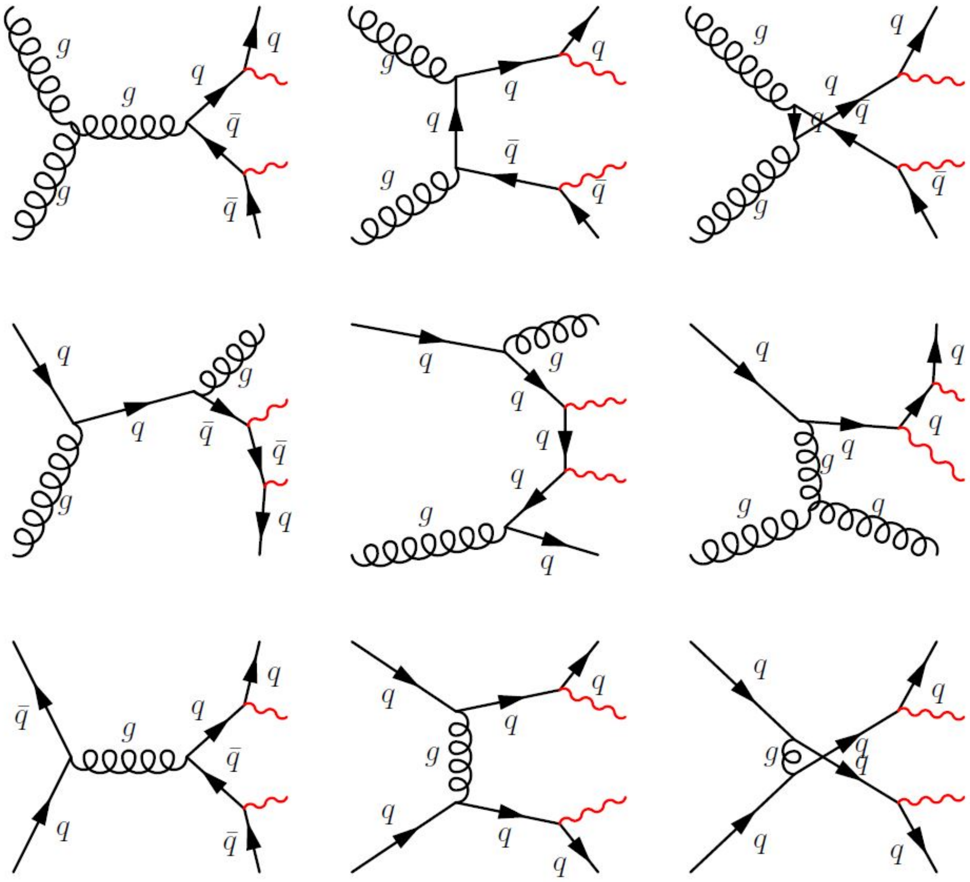

Figure 2.2: Representative Feynman diagrams for the strong production of two photons in proton-proton collisions in leading order. Photons are shown in red. The q represents any quarks or quark combination for which those processes can exist.

From there, it can already be seen that the strong processes will most likely have a higher cross-section, since they include more processes and some processes initiated by gluons which are much more likely to get from the protons. Therefore, a selection must be applied in such a way, that the electroweak processes, in particular the one with the quartic vertex, can be observed significantly.

2.2 Large Hadron Collider and ATLAS Detector

To make the later simulated data relatable, it can be useful to scale it to the actual expectation from the LHC Run 2 Data. Furthermore, in the event selection, the attributes of the ATLAS detector have to be considered, so that immeasurable events from the simulation can be excluded. Therefore, some information about the experimental setup is given below.

Large Hadron Collider (LHC)

The LHC [1, 2] first started running in 2008 with the goal to find answers to the unexplained phenomena of the Standard Model of particle physics. It is a 27km long accelerator ring in which protons are collided with each other nearly at the speed of light. Large detectors like CMS or ATLAS(see below) are used to track the collisions. In 2015, the LHC started into Run 2 with higher energy and luminosity than before. The luminosity can be calculated from the beam parameters and determines the number N of events occuring for a process with the cross section σ. It is differentiated between the instantaneous luminosity $\mathcal{L}$ and the integrated luminosity L:

$$\frac{dN}{dt} = \sigma \cdot \mathcal{L}(t) \qquad \Rightarrow \qquad N = \sigma \int_{t_0}^{t_1} \mathcal{L}(t) dt = \sigma \cdot L \tag{2.1}$$

The instantaneous luminosity is always measured parallel to the collision processes. When Run 2 ended in 2018, the LHC had delivered 139/fb [3] integrated luminosity for the ATLAS experiment. Throughout this thesis, this value is used to convert the simulated cross-sections into the expected event numbers from LHC Run 2.

ATLAS Detector

One of the most important detectors at the LHC is the ATLAS [4] detector. Since the data simulated in this thesis has to be compatible to the ATLAS measurements, it is useful to look at the detection of particles in the ATLAS experiment, in this case especially photons and partons from the processes described in section 2.1. Both are detected with the calorimeter system (fig. 2.3) of the ATLAS detector. The observables for particles measured with the detector are defined with the beam axis and the collision point. Mainly used are the transverse momentum p_T(perpendicular to the beam axis), the azimuthal angle ϕ in the transversal plane and the pseudorapidity η defined using the angle to the beam axis θ: $\eta = -\ln(\tan(\theta/2))$. Together with the measured energy deposited in the calorimeter systems the particles can be fully reconstructed. Also used throughout this thesis are the rapidity y, defined by the particle energy E and momentum along the beam axis p_z, and the angular distance ΔR:

$$y = \frac{1}{2} \ln \frac{E + p_z}{E - p_z} \qquad \Delta R = \sqrt{(\Delta\eta)^2 + (\Delta\phi)^2} \tag{2.2}$$

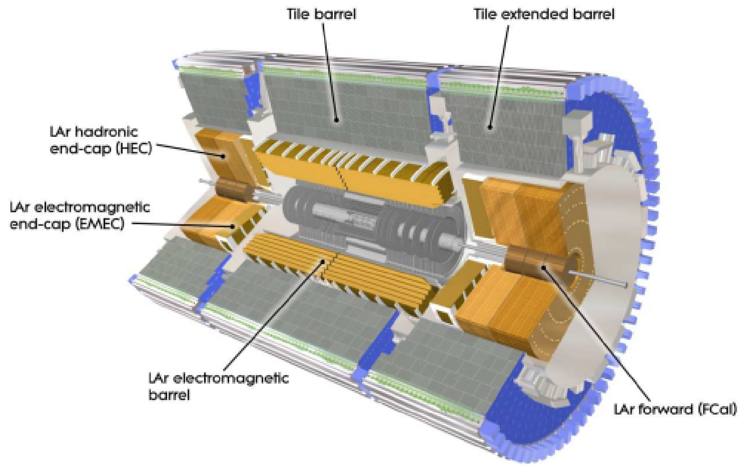

Figure 2.3: Cut-away view of the ATLAS calorimeter system, figure from [4]

While the inner detector uses magnetic fields and measures the track to obtain the transverse momentum, the main information about the particles involved here come from the electromagnetic or hadronic showers which are induced by the photons or partons. The inner layers measures electromagnetic showers induced by photons or electrons while the outer layer of the calorimeter system measures the hadronic showers. Since the detector has a cylindrical shape, the calorimeters consist of a barrel section and an end-cap. For the electromagnetic calorimeter, all of them are liquid argon calorimeters. An absorber, for example the used lead, induces the shower and this shower then ionizes the argon which can be measured by the detector cells. All the energy deposited can be used to reconstruct the jet up to the original parton. The detector uses an accordion shape to guarantee uniform ϕ segmentation. The outer barrel is a tile calorimeter using steel as absorber and scintillators to detect the particles. The end-caps for the hadronic detection are using liquid argon again. Additionally to the barrels and end-caps, a forward detector is fitted to measure pseudorapidity ranges up to 4.9. It uses copper or tungsten as an absorber and has one module for electromagnetic and 2 for parton showering. As can be seen from this setup, the particles that can be measured must have a certain pseudorapidity to be detected. It is also possible that certain regions of the detector where different modules are next to each other have to be excluded for a proper measurement. Furthermore, the particles must have a certain amount of energy or p_T, to induce the showering in the first place. As presented in section 3.2, all this must be taken into account for the simulated events as well and will therefore have to be implemented within the event analysis.

3 Methods

3.1 Monte-Carlo Event Generation

To compare the Standard Model predictions to the experimental observations, it is useful to simulate the experiment based on the theory. Used for this thesis is the event generator SHERPA [5, 6] (version 2.2.12). The event generation works by simulating and calculating different stages of the experimental processes. First is the proton-proton collision, which takes into account the beam energy and different parton distribution functions from [7]. From the partons, the hard process is simulated by calculating the scattering matrix element via integration over the phase space. After the hard process, secondary processes, hadronic showers, hadronization and decay are taken into account to mimic the actual observations from a detector. All of this is included in SHERPA, only the process has to be specified and some settings have to be specified to improve the performance. The used setup for this this thesis is presented below.

For the evaluation of the sensitivity of the electroweak measurement, it is necessary to simulate both the electroweak and the strong processes as described in section 2.1. The basic setup presented below is the same for both, the differences are discussed later. The SHERPA run cards are shown in the appendix. All simulations in this thesis are performed for only leading order processes. The chosen hard processes always have two partons as initial state and 2 photons plus additional jets in the final state. As the main matrix-element generator Comix [8] is used. Amegic [9] is only used secondary to check the processes found by Comix manually. If any Loop-induced processes were to be found, the OpenLoops [10] module would be used for those. The generated events are weighted. To relate to the LHC Run 2, the incoming proton beams are configured with an energy of 6.5 TeV each, adding up to the center of mass energy of $\sqrt{s}$ = 13 TeV. The integration of the matrix element is performed with minimum iterations of 25000 and an integration error of 5%. Numerous settings for speed and integration improvement are set by: METS_BBAR_MODE=5;CDXS_VSOPT=5; CORE_SCALE=VAR{Abs2(p[2]+p[3])};PP_RS_SCALE VAR{0.25*sqr(PPerp(p[2])+PPerp(p[3]))}; For the renormalization scales, the default scales in STRICT_METS mode are used. The EXCLUSIVE_CLUSTER_MODE is activated, making sure that only QCD-processes are assumed during jet reconstruction which means that none of the simulated photons come from the parton showering. For merging multiple jet samples "CKKW sqr(QCUT/E_CMS)/(1.0+sqr(QCUT /0.6)/Abs2(p[2]+p[3]));" is used. Furthermore, some selectors are already applied before the analysis, including $p_T > 20$ GeV of the leading and $p_T > 18$ GeV of the subleading photon, isolation of each photon (less than 2 GeV in $\Delta R < 0.1$ smooth cone with exponent 0.1) and the separation of the photons ($\Delta R > 0.2$). These selections are less strict than the ones used in the analysis but they provide more sampled events passing the analysis criteria. The analysis can by run on the fly and is described in section 3.2.

The differences for the electroweak and the the QCD setup are now discussed below. While in the electroweak setup (order: 4 EW, 0 QCD vertices) the hard process final state is given by 2 photons and exactly 2 jets (partons), the QCD setup (order: 2 EW, up to 2 QCD vertices) has 2 photons and up to 2 jets specified. To get more events with at least 2 jets, which are the ones of interest, the processes with 2 jets are enhanced by the factor 100. The electroweak setup has an additional selector requiring at least 2 jets over 20 GeV transverse momentum to be found with FastJet [11] using the anti-k_T algorithm[12] with a radius parameter of 0.4, very similar as it is done within the analysis later on. Also the electroweak setup uses the CSS_CSMODE ensuring that the 2 incoming partons do not exchange any color charge, which they should not do in any process shown in fig. 2.1. This has consequences for the simulation of the parton shower and the reconstruction of the jets since it excludes further interaction. With these setups the integration is performed in a few hours. First 1 million events are generated with the integration results to do the analysis optimizations and later, 100 million events will be used to get more precise results and smoother plots. The simulations used for chapter 6 are very similar apart from the hard processes final states and process order, which will include up to 3 jet final states and up to 1 more order of QCD vertices. Enhanced in the QCD setup will be 2 and 3 jets in the final state.

3.2 Analysis

The Analysis of the generated events was performed with the Rivet analysis toolkit[13]. This allows to select relevant events and calculate observables, which then can be plotted into histograms. For this thesis, a new analysis [14] was written, based on [15] and [16]. The criteria for event selection are described below. First, the events that can not be detected well need to be excluded. Therefore, the following conditions are introduced. The absolute pseudorapidity of each photon must be below 2.37 to be in the detector and not between 1.37 and 1.52 (see [17] and section 2.2). To identify and distinguish two photons, one of them is required to have a transversal momentum of at least 40 GeV while another must have a p_T larger than 30 GeV. Additionally, they have to separated from each other and the jets by $\Delta R > 0.4$. The photon isolation is checked by the total momentum in a $\Delta R < 0.4$ cone around the photon, which has to have an energy less than 4 GeV. Finally, the transversal momentum of the diphoton system is required to be more than 20 GeV.

For the jets the absolute rapidity must be less than 4.4 and the transversal momentum has to be larger than 25 GeV. They are reconstructed using the anti-kt algorithm [12] with a radius parameter of 0.4 and analyzed with the FastJet toolkit [11]. They also require some separation, quantified by the absolute rapidity difference. This condition will be used in the next category of cuts, the ones used to reduce the QCD background.

These selection criteria, in particular the transversal momentum of the two leading jets $p_{T;j}$, the invariant mass of the dijet system m_{jj}, the leading jets absolute rapidity difference Δy_{jj}, and the centrality ξ

$$\Delta y_{jj} := |y_{j1} - y_{j2}| \qquad \xi := \frac{|y_{\gamma\gamma} - \frac{1}{2}(y_{j1} + y_{j2})|}{\Delta y_{jj}} \tag{3.1}$$

are not finally chosen so far. These cuts must be optimized to obtain a high EW-signal against the QCD background (see chapter 4). To start with, they are chosen as in [18]; $p_{T;j} > 80$ GeV, $\Delta y_{jj} > 2$, $m_{jj} > 1000$ GeV and $\xi < 1.0$. In every case, the event is selected if exactly two photons and at least two jets pass all these criteria. For all of those passed events, numerous observables can be computed and histograms are plotted of the differential cross section depending on the observable. Together with the LHC luminosity, this can then be used to compare the simulations to the actual data.

4 Analysis Optimization

As mentioned earlier, the analysis of the simulated events must be optimized to obtain a high electroweak signal against the QCD background. To quantify this sensitivity, the significance is introduced as the quotient of the number of expected signal events S and the statistical deviation of the expected background event number B:

$$\Sigma := \frac{S}{\Delta_{stat} B} = \frac{S}{\sqrt{B}} \tag{4.1}$$

Here, a Poisson distribution is assumed. It can therefore be stated, that a high significance will increase the level of certainty the signal can be measured with. A significance over 5 will be enough to conclude that a signal is indeed measured. To calculate and optimize it, the expected number of signal and background events must be known. It can be calculated for the LHC Run 2 as the product of the integrated luminosity of $L = 139\frac{1}{fb}$ [3] and the total cross-section of the cut process. The latter is obtained from the simulation and the event selection by multiplying the sum of the passed event weights with the total cross section given by SHERPA and dividing by the sum of the weights before the selection.

4.1 ROOT Analysis

The optimization is performed in 2 iterations. In each of them one cut parameter is varied while the others stay fixed. After doing this for all 4 parameters (transversal momentum of the two leading jets $p_{T,j1}$ and $p_{T,j2}$, leading jets absolute rapidity difference Δy_{jj} and invariant mass of the dijet system m_{jj} must be larger than their initial cuts, centrality ξ must be smaller than the cut), the value with the highest significance for each parameter is chosen as the base for the next iteration. The main issue with that however is time, since the Rivet analysis takes a lot of time to run due to the need to reconstruct the jets. To make this faster, a new analysis with ROOT [19] is written [14], where the event is only analyzed on the hard process at parton level. The event data is converted using Delphes[20] with the ATLAS detector card. By using this method, all information of the parton shower and hadronization may be neglected which improves the run time greatly (from around 10 ms/event to 1μs/event), but limits the accuracy. At first the starting values are chosen as in section 3.2. From the first iteration of each parameter, where the significance is calculated by ROOT for different cuts, the values for the next iteration are chosen. Not always is it sensible to simply choose the maximum, a compromise between the significance and the total expected event number has to be made. If the latter is too low, then it is possible that the real ATLAS data will not contain enough events for conclusions. That is why, if possible, the cut is chosen to sort out less events while still having a high significance. To visualize this issue, an error on the significance is introduced, assuming a Poisson distribution for the events:

$$\Delta_P\Sigma = \sqrt{\left(\frac{\partial\Sigma}{\partial S}\sqrt{S}\right)^2 + \left(\frac{\partial\Sigma}{\partial B}\sqrt{B}\right)^2} = \Sigma\sqrt{\frac{1}{S} + \frac{1}{4B}} \tag{4.2}$$

This of course does not produce independent statistical errors for the significance, because the underlying simulation is the same, but it gives and impression of the reliability of certain calculated significance values. More than one iteration is also necessary because there might be some correlation between the different cuts. With all this, fig. 4.1 and table 4.1 can be produced. As mentioned above, it may be unpractical to simply choose the maximum of the significance. Especially for the jet separation and the centrality, the values were chosen to be less strict on the event selection rather than give maximal significance to obtain more events. In case of the $p_{T,j}$ cut, the significance remains high for the interval between 20 and 70 GeV. In this case the data is insufficient to make a definite conclusion about the cut position, it is therefore made at a local maximum of the significance at the center of said interval, since this will most likely be the most applicable cut for different data sets. In case of the jet separation, it seems to have a higher significance for higher cuts. However, that also excludes more events, which would make the result less trustworthy. The choice is made for one of the last cut values before fluctuations get to high ($\Delta y_{jj}^{cut} > 4$). The other 2 selection parameters can be chosen quite directly by choosing the maximum of the significance where the least events get cut out. For the centrality, the fluctuating values of significance for the low cuts are again not chosen, since they exclude too many events. A third iteration could of course be performed, but because the cut values change considerably less after the first iteration and the parton level analysis limits the results accuracy anyway, the values after two iterations are deemed precise enough.

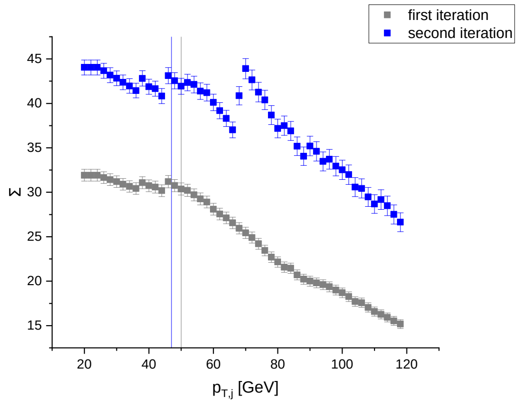

(a) leading jets transverse momentum cut $p_{T,j}$

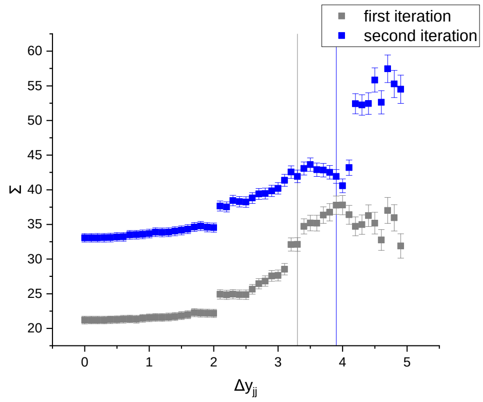

(b) leading jets absolute rapidity separation Δy_{jj}

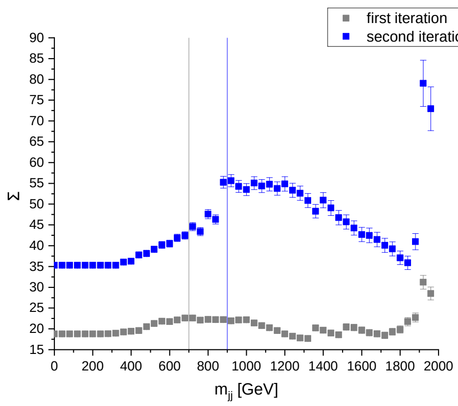

(c) dijet invariant mass m_{jj}

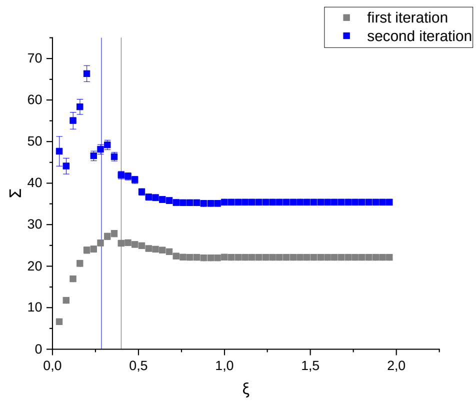

(d) centrality ξ

Figure 4.1: Significance of the electroweak signal in dependence of the cut values of the respective observable in two iterations, calculated at parton level with ROOT. The chosen values after each iteration are shown as vertical line.

	$p_{T,j}/GeV >$	$\Delta y_{jj} >$	$m_{jj}/GeV >$	$\xi <$
start values	80	2.0	1000	1.0
after first iteration	50	3.3	700	0.4
after second iteration(final)	47	3.9	900	0.3

Table 4.1: chosen cut values for the event selection after each iteration depicted in fig. 4.1

4.2 Validation with Rivet

In any case, it should be mentioned that the actual values of significance will be much lower than the ones shown in fig. 4.1, due to the simple analysis at parton level. The real results will be obtained by the Rivet analysis where the jets are reconstructed from the parton shower. This means, the previous results and findings should be validated by performing similar steps with the rivet analysis, but as mentioned earlier, that will consume too much time. Therefore, a different approach is used here, to validate the results for the m_{jj} and the centrality cut. First, with the Rivet analysis, histograms are produced for the simulation data of the electroweak and QCD process for m_{jj} and the centrality, in each case without any corresponding cut. The other cut values are chosen as the optimized ones (see table 4.1) and the rest as described in section 3.2. The result are histograms describing $\frac{d\sigma}{dm_{jj}}(m_{jj})$ or $\frac{d\sigma}{d\xi}(\xi)$. To make the analysis of the effect of different cuts quick, functions are introduced to describe the data from the histograms:

$$\begin{aligned} \frac{d\sigma}{dm_{jj}} &= \exp\left(a_0 + a_1\frac{m_{jj}}{GeV} + a_2\big(\frac{m_{jj}}{GeV}\big)^2 + a_3\big(\frac{m_{jj}}{GeV}\big)^3\right) \cdot \frac{pb}{GeV} \\ \frac{d\sigma}{d\xi} &= \exp\left(b_0 + b_1\xi + b_2\xi^2\right) \cdot pb \end{aligned} \tag{4.3}$$

With the fit parameters a_i and b_j. The functions themselves are chosen to be the least complicated, but still describing the general behaviour of the data. The fit quality and results are shown in fig. 4.2 an table 4.2.

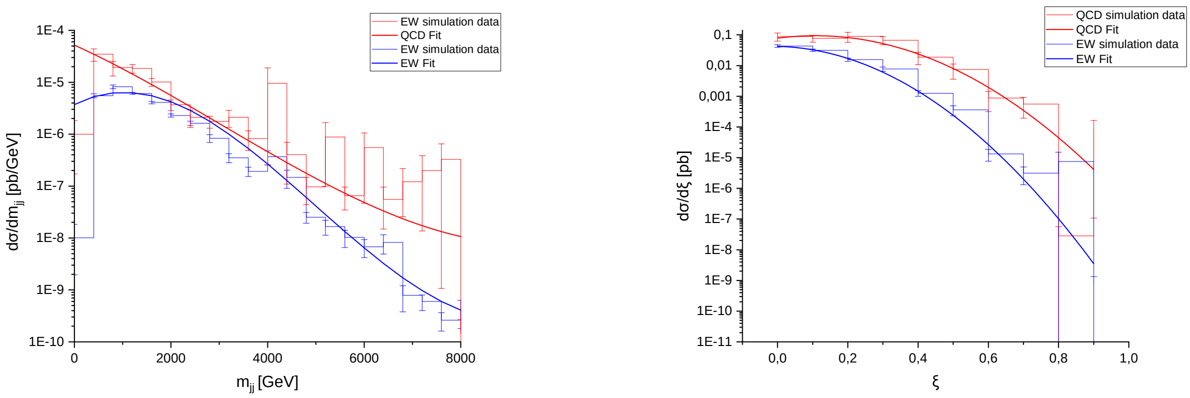

(a) dijet invariant mass m_{jj}, 8 million simulated events

(b) centrality ξ, 1 million simulated events

Figure 4.2: Histograms of the simulated data of the differential cross-section depending on the respective observable. The fitted functions (eq. (4.3))are shown as lines (see table 4.2).

fit parameter	a_0	a_1	a_2	a_3	b_0	b_1	b_2
electroweak process	-12.5	11e-4	-6e-7	4e-11	-3.17	-0.7	-19.4
strong/QCD process	-9.87	-9.7e-4	-9.4e-8	1e-11	-2.55	3.4	-15.95

Table 4.2: fit results for the data shown in fig. 4.2 to the functions eq. (4.3)

This being just a qualitative discussion of the accuracy of the values obtained by ROOT, the fit uncertainties are not mentioned here, they do however are of a noticeable size, especially for the m_{jj} fit. That would also influence the result for the optimal cut value, which is a problem with this method. As it is used just as validation, it is acceptable for now, but for further analyses this would have to be improved by simulating more data and using more accurate fit functions. With these fitted functions, the calculation of the significance is very straightforward, because the expected signal and background events can be obtained by integrating these functions:

$$\begin{aligned} S(m_{jj;cut}) &= L \cdot \sigma^{ew}(m_{jj;cut}) = L \int_{m_{jj;cut}}^{\infty} \frac{d\sigma^{ew}}{dm_{jj}} dm_{jj} \approx L \int_{m_{jj;cut}}^{10TeV} \frac{d\sigma^{ew}}{dm_{jj}} dm_{jj} \\ S(\xi_{cut}) &= L \cdot \sigma^{ew}(\xi_{cut}) = L \int_{0}^{\xi_{cut}} \frac{d\sigma^{ew}}{d\xi} d\xi \end{aligned} \tag{4.4}$$

Since a numerical integration is performed, the upper integration border of the m_{jj} cut function is set to 10 TeV. This is reasonable because the data suggests that almost no events are expected above $m_{jj} = 8$ TeV and the the centre of mass energy is not much higher with $\sqrt{s} = 13$ TeV. The same formulae apply for the background with the QCD cross-sections and according fit functions. The results for the significance are presented in comparison to the results from the according ROOT analysis. The significance values with this method are much closer to a real result since the Rivet analysis considers all parts of the processes, but also not exact due to the uncertainty of the fit functions. From fig. 4.3, it becomes clear that the ROOT analysis seems to produce the same significance behaviour for these two cuts as the Rivet analysis. Although the chosen cut values do not match the optimal value predicted from Rivet exactly, they are also not far from one another. Certainly, this is an indicator that the previously chosen optimal cuts are sensible.

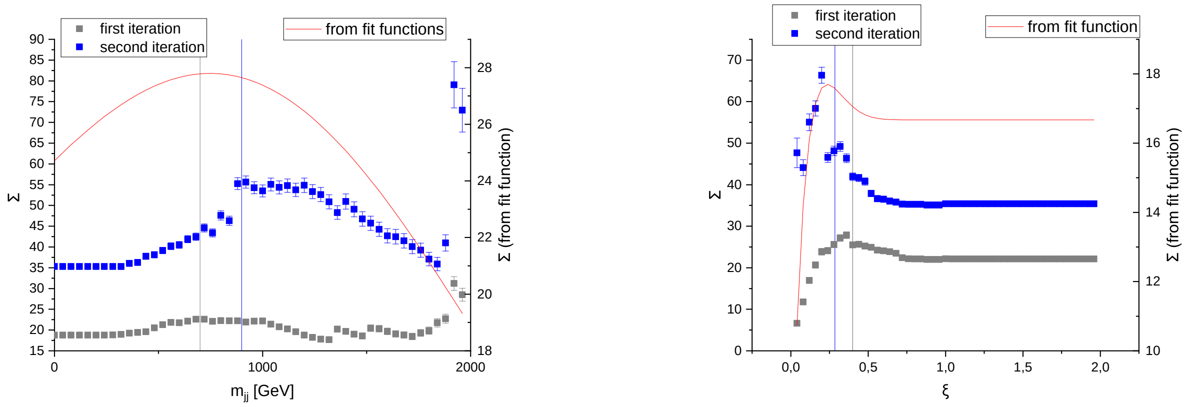

(a) dijet invariant mass m_{jj} **(b)** centrality ξ

Figure 4.3: Significance of the electroweak signal in dependence of the respective observable as given by ROOT in 2 iterations and as predicted by the Rivet analysis and according fit functions. The chosen values after each iteration are shown as vertical line.

4.3 Multiple Bin Significance

So far, the significance has been calculated by the number of expected events that pass the selection, when it might be better to divide them into two (or more) bins where they are sorted into by a certain observable. The resulting significance would be calculated from the significance values of the two individual bins since they are statistically independent:

$$\Sigma_{tot} = \sqrt{\Sigma_1^2 + \Sigma_2^2} \tag{4.5}$$

Whether this might lead to a noticeable improvement should be tested. For that, the two observables m_{jj} and ξ are used again. Additional to the cut, a so called edge value is introduced, so that all events that pass the cut are categorized by having the observable below or above the edge. To calculate the significance in each bin, the fit functions (eq. (4.3), table 4.2) are used again. This provides a smooth behaviour of significance and can be implemented quickly, as the event numbers for the two bins can be calculated as follows:

$$\begin{aligned} S_1(m_{jj;cut}, m_{jj;edge}) &= L \int_{m_{jj;cut}}^{m_{jj;edge}} \frac{d\sigma^{ew}}{dm_{jj}} dm_{jj} \\ S_2(m_{jj;cut}, m_{jj;edge}) &= L \int_{m_{jj;edge}}^{10TeV} \frac{d\sigma^{ew}}{dm_{jj}} dm_{jj} \\ S_1(\xi_{cut}, \xi_{edge}) &= L \int_{\xi_{edge}}^{\xi_{cut}} \frac{d\sigma^{ew}}{d\xi} d\xi \\ S_2(\xi_{cut}, \xi_{edge}) &= L \int_{0}^{\xi_{edge}} \frac{d\sigma^{ew}}{d\xi} d\xi \end{aligned} \tag{4.6}$$

It is calculated accordingly for the background events with the QCD cross-section fit function. With this, the significance can be calculated within each bin and then put together to the total significance in dependence of the cut and edge value. To compare the results, the maximum significance for the one bin approach is read from fig. 4.3. It is predicted to be 27.8 from the m_{jj} fits and 17.7 from the centrality fit. From fig. 4.4 the maximum total significance can be read. It is below 30 for the dijet invariant mass and below 18.5 for the centrality. That would be less than 8% improvement for both observables. This method takes a high effort, which would be even higher for the usage of more than 2 bins, so this improvement is too little to justify that. Also, the optimal cut values might change for a different number of bins used. For the 2 bins here, the optimum changes for the m_{jj} cut to 400 GeV while the optimal ξ cut remains at roughly the same as in fig. 4.3. This means that for a multiple bin optimization, all steps will have to be repeated to ensure the best signal sensitivity. The significance will therefore be calculated with one bin as before. However, this method could be used in further work where the slight improvement is necessary.

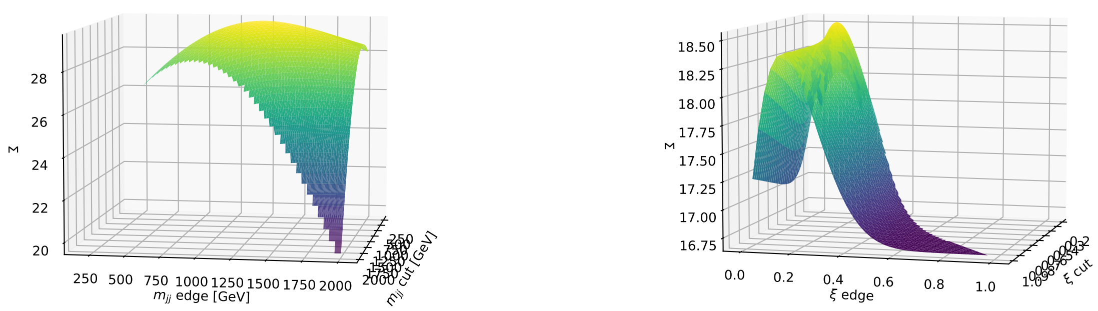

(a) dijet invariant mass m_{jj} **(b)** centrality ξ

Figure 4.4: Total significance in dependence of the cut and the bin edge between the 2 bins for the named observables, predicted by the fit functions from eq. (4.3),table 4.2

4.4 Additional Gap Jet Cut

As in [18], an additional criterion for separating the electroweak signal from the background could be the number of jets N_{gap} in the rapidity interval between the rapidity of the 2 jets with highest transversal momentum. Without cutting events for this observable, it can be calculated by Rivet and shown as a histogram (see fig. 4.5). From there, it can be concluded that the electroweak processes are much more likely to have $N_{gap} = 0$ than the QCD processes. Therefore, a new cut where this gap jet number must be zero for the event to pass could be introduced. The results for this central jet veto in terms of significance, along with other results from this section, is shown in table 4.3. It should be mentioned that the shown uncertainties are statistical ones from the simulation, not the expected uncertainties for the event observation, which is assumed as a Poisson distribution. Therefore, the ones presented here can be reduced by more simulation data while the expected uncertainty of $\sqrt{B}$ used to calculate the significance (see eq. (4.1)) can not. For the significance, they are calculated using Gaussian error propagation (eq. (4.7)).

$$\Delta\Sigma = \Sigma\sqrt{\left(\frac{\Delta S}{S}\right)^2 + \left(\frac{-\Delta B}{B}\right)^2} \tag{4.7}$$

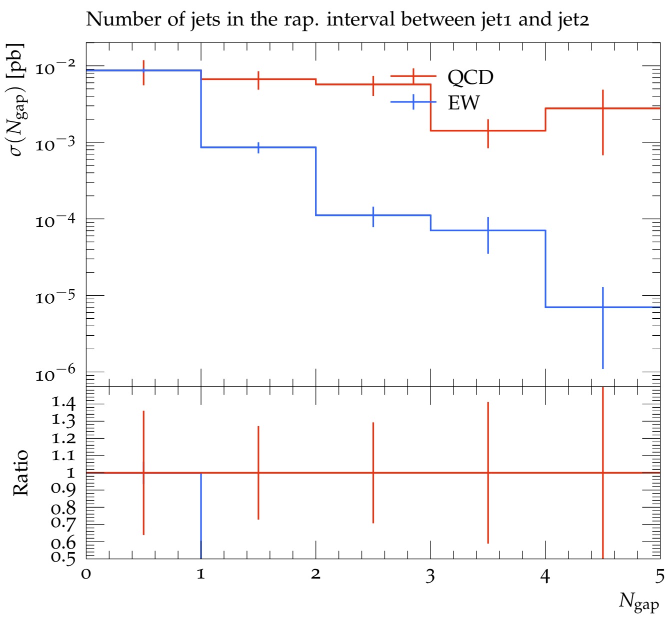

Figure 4.5: Differential cross-section in dependece of the number of jets N_{gap} in the rapidity interval of the leading p_T jets of the QCD and EW diphoton+jets production with the optimized cuts described in table 4.1 and section 3.2 for 1M simulated Monte-Carlo events.

	MC-events		expected events (139/fb)		significance
cuts/event selection	QCD	EW	QCD	EW	(of EW signal)
before optimization	0.8%	2%	4600 ± 600	950 ± 60	14.0 ± 1.3
after optimization	0.1%	1.1%	3500 ± 600	1260 ± 80	21.3 ± 2.3
with 100M generated events			3790 ± 120	1183 ± 7	19.22 ± 0.32
optimized and $N_{gap} = 0$	0.04%	0.6%	1200 ± 400	1150 ± 70	33 ± 6
with 100M generated events			1000 ± 50	1040 ± 7	32.9 ± 0.9

Table 4.3: Passed MC-events, expected events for LHC Run 2 at 139/fb [3] and calculated significance (eq. (4.1), eq. (4.2)) for different event selection setups described throughout section 3.2 and chapter 4. If not specified otherwise, the numbers are obtained from 1M generated events.

From there, it can clearly be concluded that the additional central jet veto is leading to a much better significance. It is also shown that much less of the QCD events pass the selection which leads to higher statistical errors. This is the reason why the optimization was performed without this criterion and with only 1 million generated events, since the optimization would otherwise take too much time. Although more generated events might improve the statistical certainty of the results, especially for the background, the results presented are still valid. However, for future work on the subject of this thesis, it is certainly possible to decrease the statistical deviations with more time and resources.

For further analysis, and to make sure the previous results are not changed by this cut, it is assumed that the N_{gap} criterion is uncorrelated to the other used observables for optimization. This means, the cross-sections and histograms produced without the additional cuts can be scaled down to be the ones including that cut. The scale factors are concluded from table 4.3 to be 0.26 for background events and 0.879 for signal events. The scaled down histograms for two optimization observables are compared to the ones of a full analysis with the additional cut in fig. 4.6. From this figure, much can be concluded, firstly that the assumption of no correlation between the N_{gap} observable and other observables was most likely justified. In case of the electroweak events, this clearly is the case, for the QCD processes, especially in m_{jj}, there are still high statistical fluctuations, but there is no inherent contradiction to the assumption. This means that the approach made in this section, to optimize without the central jet veto for more time effiency, was justified. In fig. 4.6, it can also be seen that even with 100 million simulated Monte-Carlo events, the statistical fluctuations are high for the QCD background. Therefore, the additional cut for $N_{gap} = 0$ is a huge improvement but does not require any changes to the previously performed analysis. Also, it is shown that the generation of enough background events for a low statistical deviation might need a lot of time and resources, since even 100M events still show fluctuations.

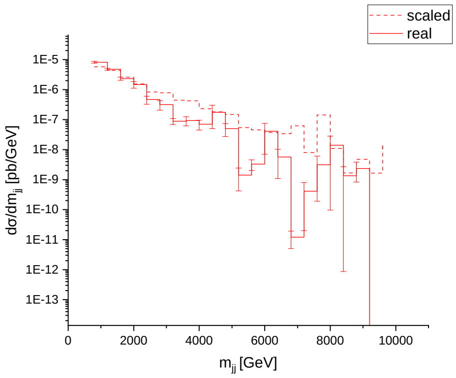

(a) dijet invariant mass m_{jj}, QCD processes

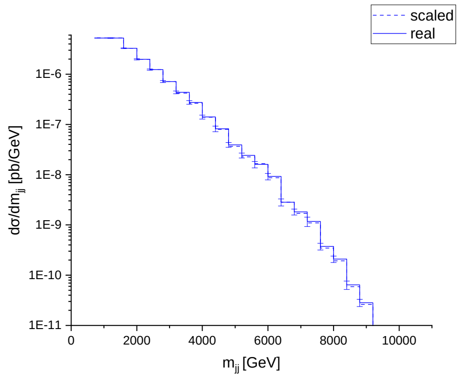

(b) dijet invariant mass m_{jj}, EW processes

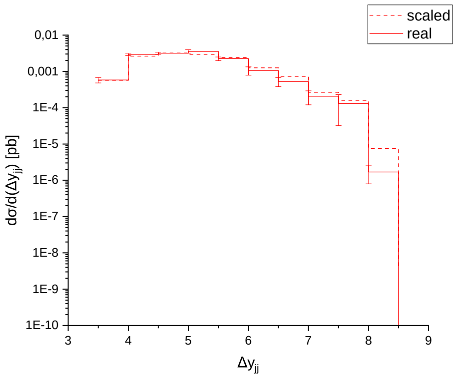

(c) centrality ξ, QCD processes

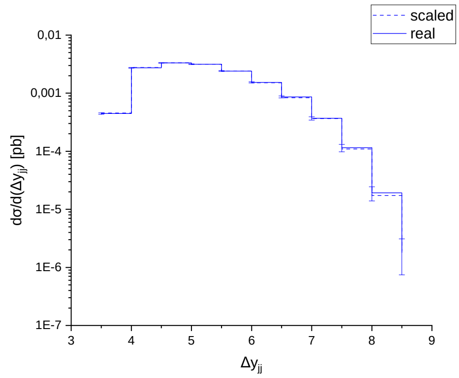

(d) centrality ξ, EW processes

Figure 4.6: Differential cross-section of the diphoton+jets production in dependence of the named observables scaled for the event selection without $N_{gap} = 0$ and the real values for the event selection with this criterion. Scaling factors are 0.26 for QCD events and 0.879 for EW events. The plots are created from a 100M Monte-Carlo events sample.

4.5 Influence of Systematic Uncertainties

Finally, the influence of systematic uncertainties on the findings in this section will be discussed. So far, only statistical uncertainties of the event numbers were assumed as coming from a Poisson distribution, but these numbers come from a Monte-Carlo simulation. This may deviate systematically from the real measured data and therefore influence the significance. Considered here is only the uncertainty on the QCD background, because this mainly drives the significance. With the significance (eq. (4.1)) being defined as the expected signal event number divided by the statistical error of the background, this can be modified to a division by the total error of the background with the systematic error being $\Delta_{sys}B := \delta_B \cdot B$:

$$\Sigma_{mod} := \frac{S}{\Delta_{tot}B} = \frac{S}{\sqrt{\Delta_{stat}B^2 + \Delta_{sys}B^2}} = \frac{S}{\sqrt{B + \delta_B^2 B^2}} \tag{4.8}$$

For some exemplary percentages δ_B, the significance in dependence of the cut values of m_{jj} and ξ is plotted using the fit functions (eq. (4.3)) from the Rivet analysis histograms in fig. 4.7. This means that those results do not include the selection for the gap jets discussed in section 4.4. If no correlation between the observable N_{gap} and the dijet invariant mass or the centrality is assumed, the calculated expected signal and background events can be scaled to the values for the included $N_{gap} = 0$ cut (see section 4.4). The resulting influence of the systematic uncertainty is presented in fig. 4.8.

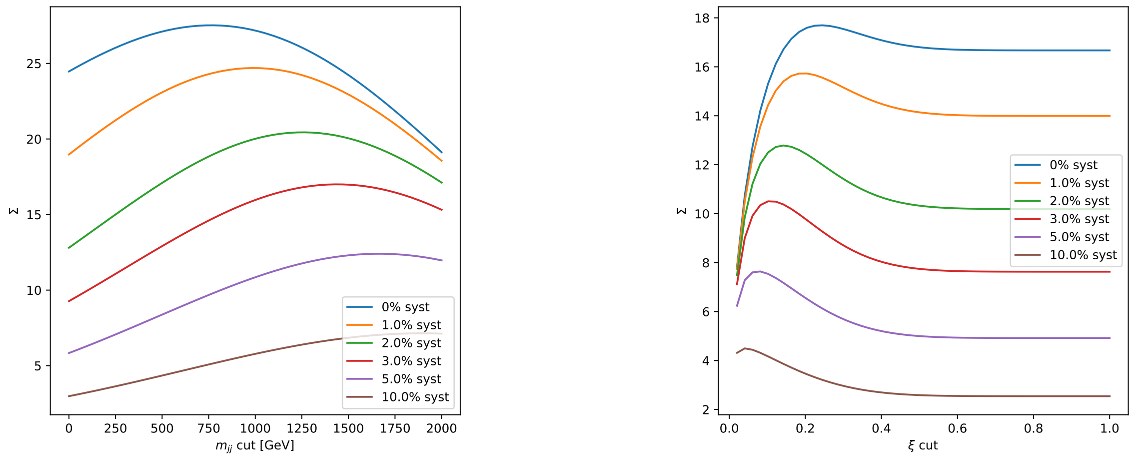

(a) dijet invariant mass m_{jj} **(b)** centrality ξ

Figure 4.7: Modified significance of the electroweak signal in dependence of the cut for the named observables with assumed percentages of systematic errors, without any cut for N_{gap}, predicted by the fit functions from eq. (4.3),table 4.2

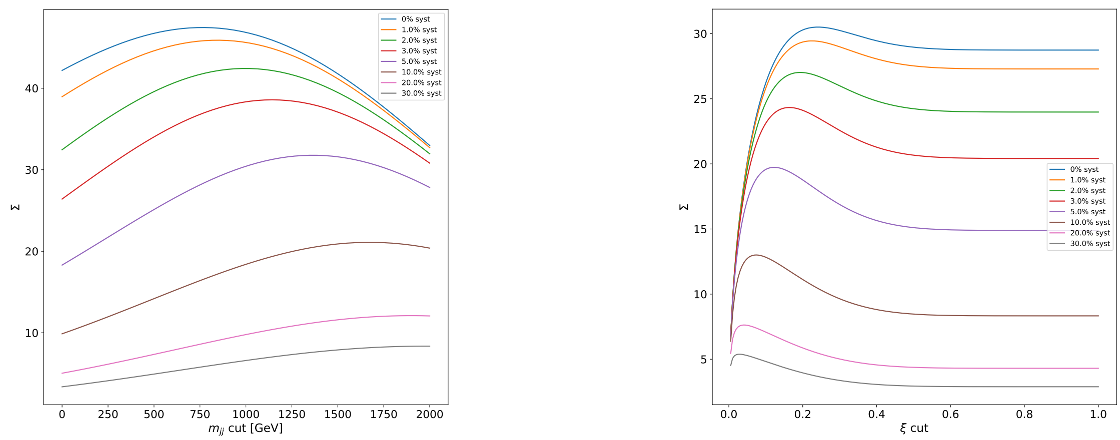

(a) dijet invariant mass m_{jj} **(b)** centrality ξ

Figure 4.8: Modified significance of the electroweak signal in dependence of the cut for the named observables with assumed percentages of systematic errors and with $N_{gap} = 0$, predicted by the fit functions from eq. (4.3),table 4.2 and scaling them down as in section 4.4.

It is shown how the additional gap jet cut improves the significance once more. Furthermore, the maximum significance corresponds to different cuts for different systematic uncertainties. This indicates that for a certain size of the systematical error, different cut values might be optimal. But because the significance drop is dominated by the existence of systematic errors, not by the shift in the significance maximum and because the shift tends to go to more strict cuts, which would exclude more events, the chosen optimized values are kept here. It is also obvious that the additional N_{gap} cut leads to a higher significance and therefore allows higher systematic uncertainties, while the general behaviour stays the same due to the assumption of uncorrelated cuts. In conclusion, for the final analysis setup with the central jet veto, a significance of over 30 can be achieved without any systematic error and the minimal required significance of 5 should still be exceeded with a high systematical error. With the expected event numbers from table 4.3 and eq. (4.8) with Gaussian error propagation (eq. (4.9) for the simulation errors, fig. 4.9 can be produced.

$$\Delta\Sigma_{mod} = \sqrt{\left(\frac{\Delta S}{\sqrt{B + \delta_B^2 B^2}}\right)^2 + \left(\frac{-\Delta B \cdot S(1 + 2\delta_B^2 B)}{\sqrt{B + \delta_B^2 B^2}^3}\right)^2} \tag{4.9}$$

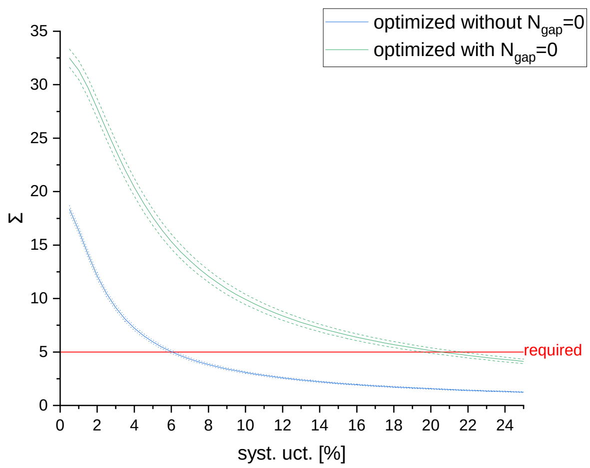

Figure 4.9: Modified significance of the electroweak signal in dependence the assumed systematic uncertainty for the expected background events with and without the additional central jet veto. In red, the required significance of 5 is shown. The event numbers are taken from table 4.3 from 100 million generated events.

This presents again the necessity of the additional gap jet cut, which allows a much higher deviation of the background. The maximum allowed systematic uncertainty of the background can be read to be around 20.5%. For a real estimation of this deviation, actual experimental data would be needed. For now, there is no reason against a measurement using the optimized criteria being sensitive for the electroweak diphoton production.

5 Histograms

In this chapter, histograms of the differential cross-section depending on different observables are shown. Some of them were already used in the optimization, others are chosen related to the photons, just to present their behaviour. In all histograms, the QCD-background is compared to the electroweak signal, but they are not used for any sensitivity study, only to demonstrate the the behaviour of different observables. The shown errors are statistical uncertainties from the simulation. All of them are produced with the optimized selection criteria discussed in chapter 4 and the central jet veto. They are now also produced with 100 million generated events.

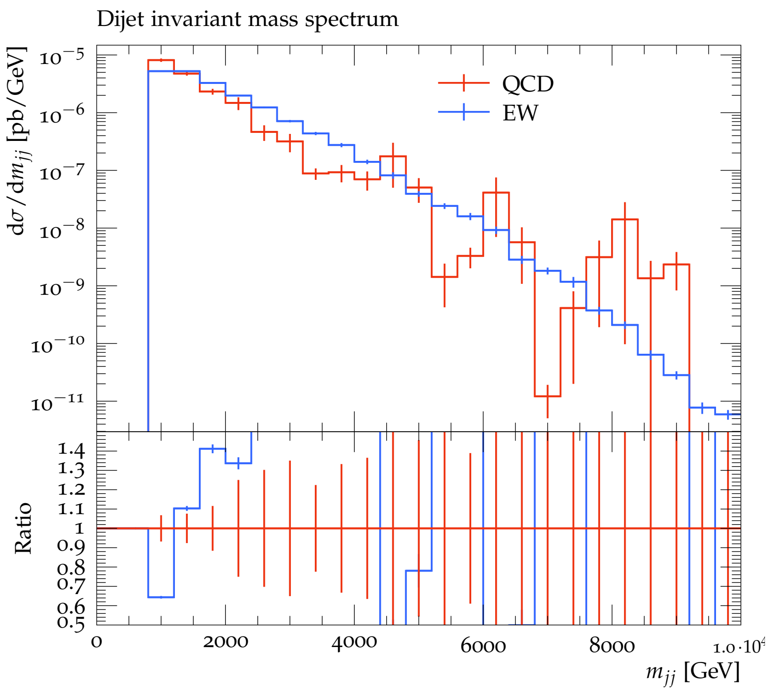

Figure 5.1: Differential cross-section for the electroweak and strong diphoton production at $\sqrt{s} = 13$ TeV compared in dependence of the dijet invariant mass from 100 million simulated events and with optimized cuts.

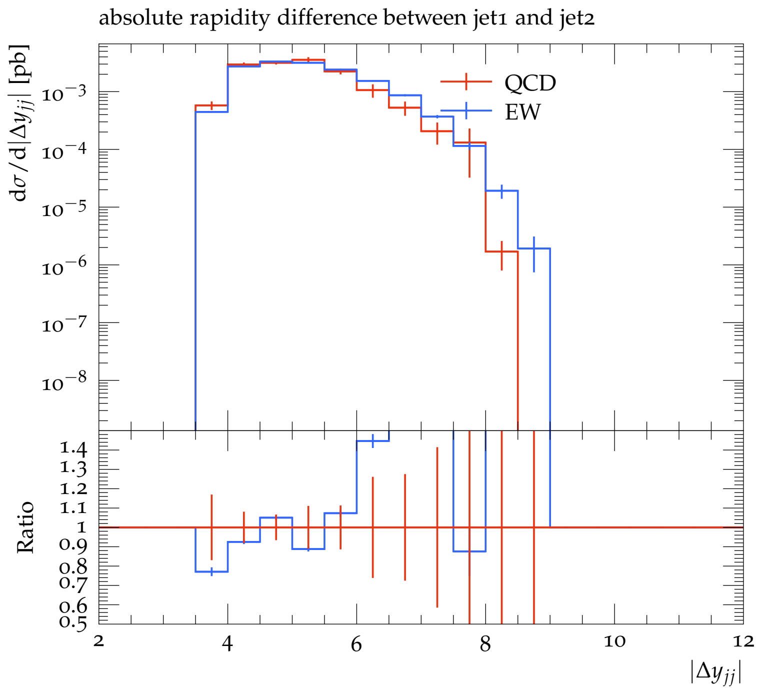

Figure 5.2: Differential cross-section for the electroweak and strong diphoton production at $\sqrt{s} = 13$ TeV compared in dependence of the leading jets absolute rapidity difference from 100 million simulated events and with optimized cuts.

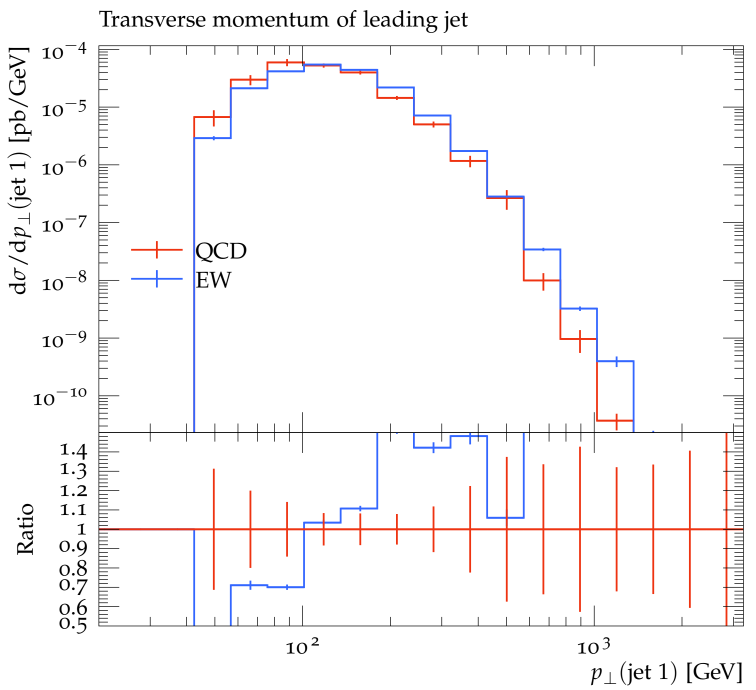

Figure 5.3: Differential cross-section for the electroweak and strong diphoton production at $\sqrt{s} = 13$ TeV compared in dependence of the transversal momentum of the leading jet (highest p_T) from 100 million simulated events and with optimized cuts.

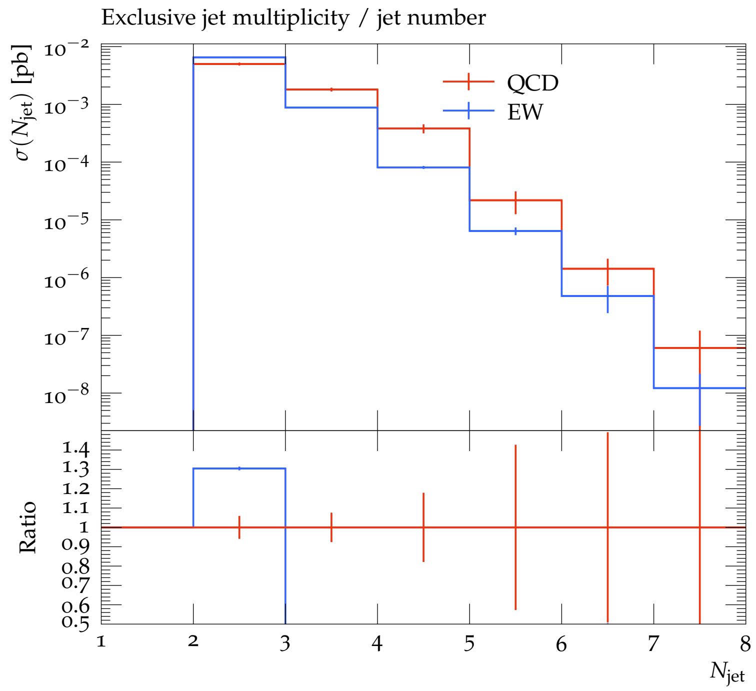

Figure 5.4: Differential cross-section for the electroweak and strong diphoton production at $\sqrt{s} = 13$ TeV compared in dependence of the number of jets from 100 million simulated events and with optimized cuts.

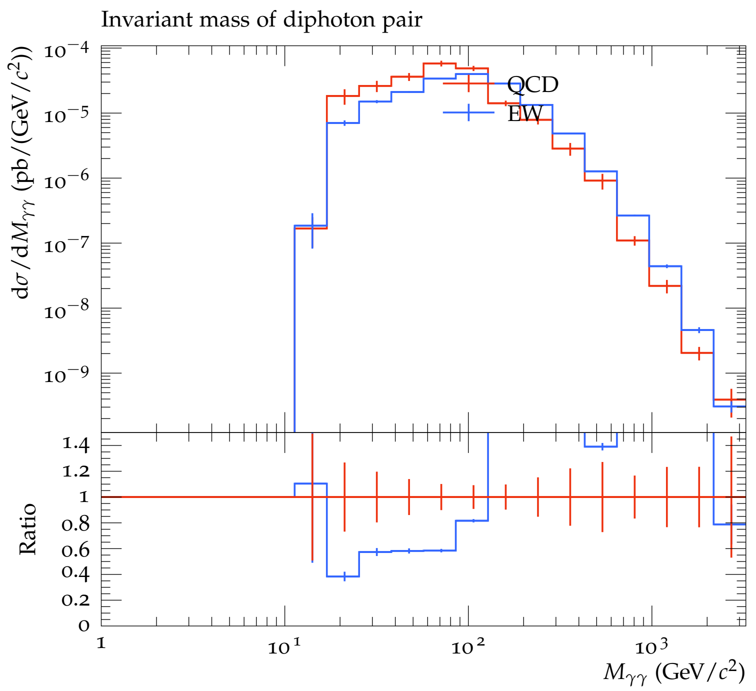

Figure 5.5: Differential cross-section for the electroweak and strong diphoton production at $\sqrt{s} = 13$ TeV compared in dependence of the diphoton system invariant mass from 100 million simulated events and with optimized cuts.

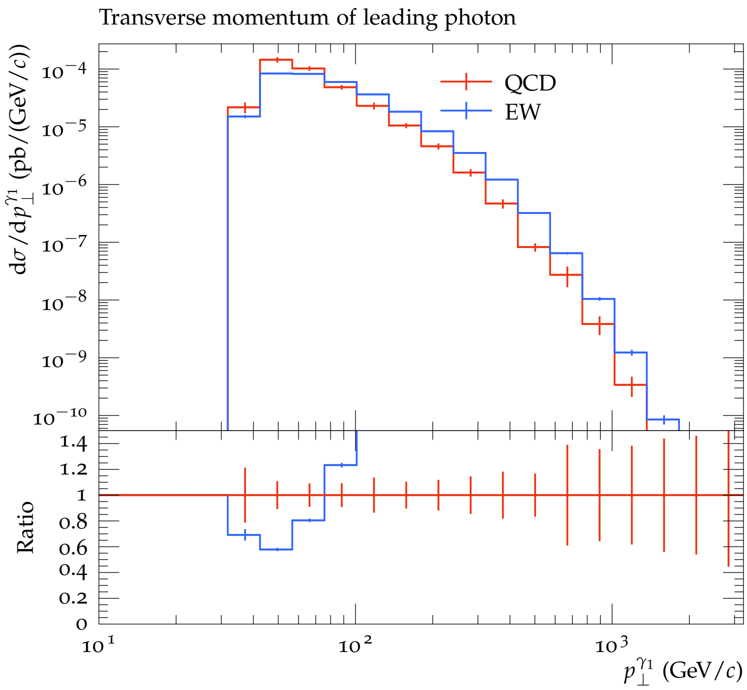

Figure 5.6: Differential cross-section for the electroweak and strong diphoton production at $\sqrt{s} = 13$ TeV compared in dependence of the transversal momentum of the leading photon (highest p_T) from 100 million simulated events and with optimized cuts.

From figs. 5.1 to 5.6, it becomes clear that, at least for the selected observables, the strong and electroweak processes have a similar cross-section and behaviour in the respective observable. The latter indicates, that there is not a much better cut option anymore since the events seem to behave similarly within the determined cuts. This is a validation of the work described in chapter 4. Once more, this also shows the much higher statistical deviations of the background events, which could only be resolved by a higher time effort in the event simulation.

6 Further Simulation

So far, all simulation has been strictly at leading order of the 2→4 process from 2 partons to 2 photons and 2 jets. To give an outlook on further possibilities of simulations the results of the event production from a setup including 3 jets at leading order is shown in this chapter. Until now, 3 or more jets could only result from the hadronization. With these setups, hard 2→5 processes are included in the integration and this should therefore be a more precise prediction of the actual processes. The rest of the event generation setup stays the same as in section 3.1 However, these more advanced setups will only be compared to the ones used so far in this thesis, to show if any changes to the previous procedures might be necessary in future work. The electroweak processes are now still defined by having exactly 4 electroweak vertices while the strong processes have only 2. Shown in figs. 6.1 to 6.4 are histograms of some observables included in the optimization and another observable of the photons, which are also shown for the previous simulation only in chapter 5. The shown errors are statistical uncertainties from the simulation. Furthermore, table 6.1 shows the change in cross-section and significance resulting from this more advanced simulation.

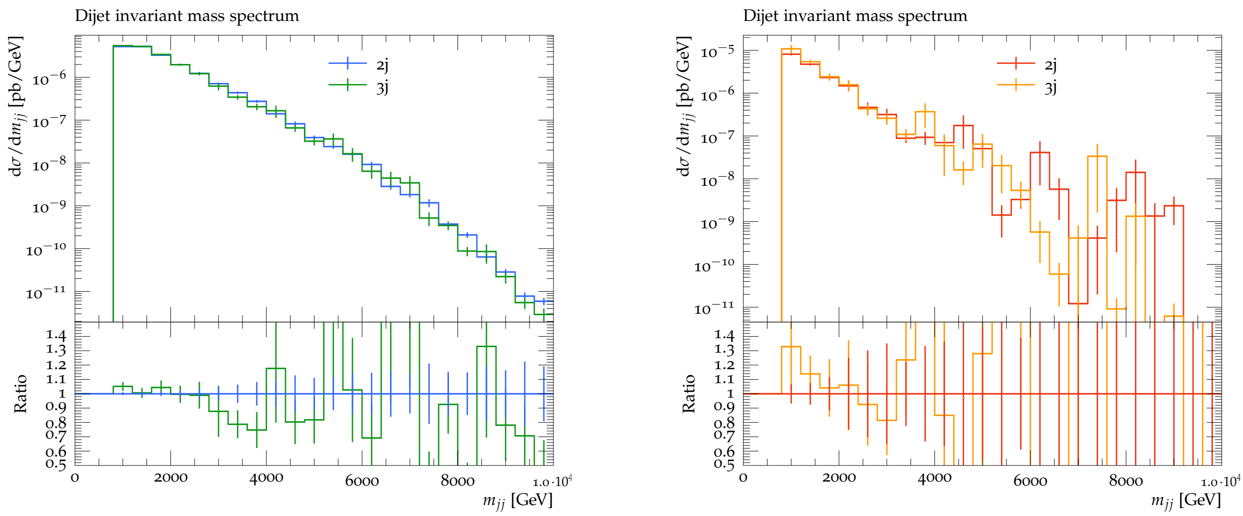

(a) electroweak signal **(b)** strong background

Figure 6.1: Differential cross-section for the diphoton production at $\sqrt{s} = 13$ TeV in dependence of the dijet invariant mass from 100 million simulated events and with optimized cuts. Compared are the used simulation including up to 2 jets in the hard process and an advanced one including up to 3 jets.

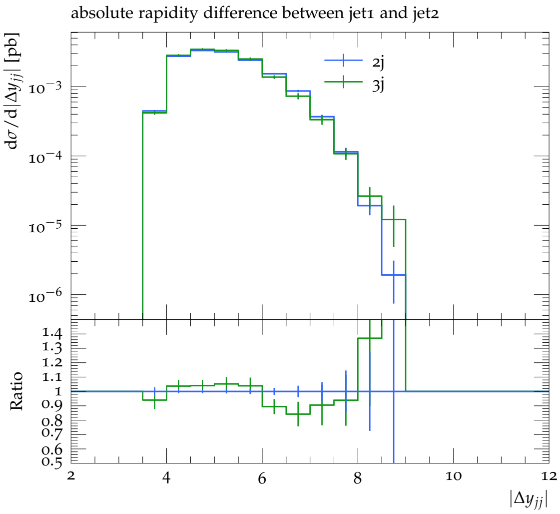

(a) electroweak signal

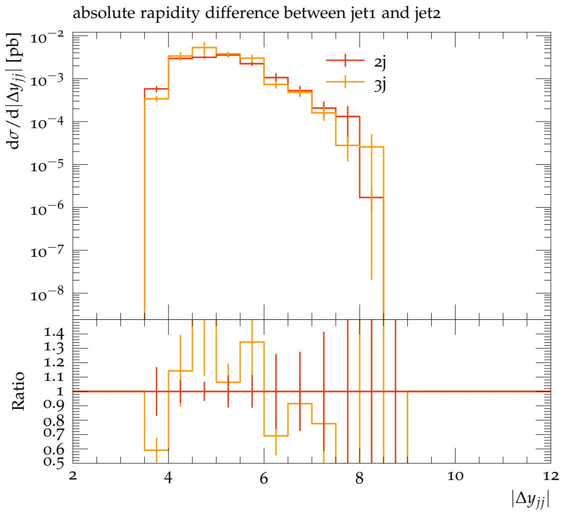

(b) strong background

Figure 6.2: Differential cross-section for the diphoton production at $\sqrt{s} = 13$ TeV in dependence of the leading jets absolute rapidity difference mass from 100 million simulated events and with optimized cuts. Compared are the used simulation including up to 2 jets in the hard process and an advanced one including up to 3 jets.

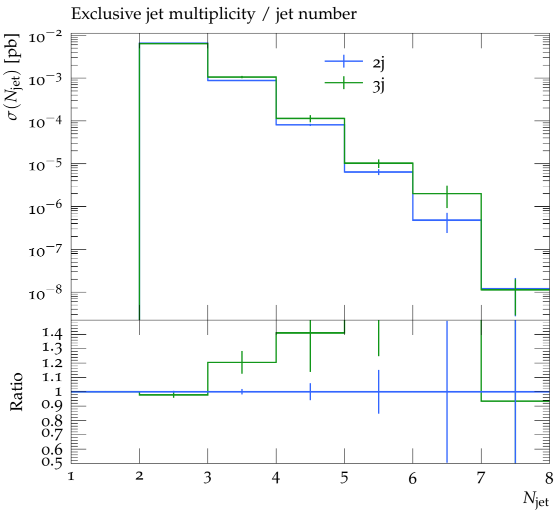

(a) electroweak signal

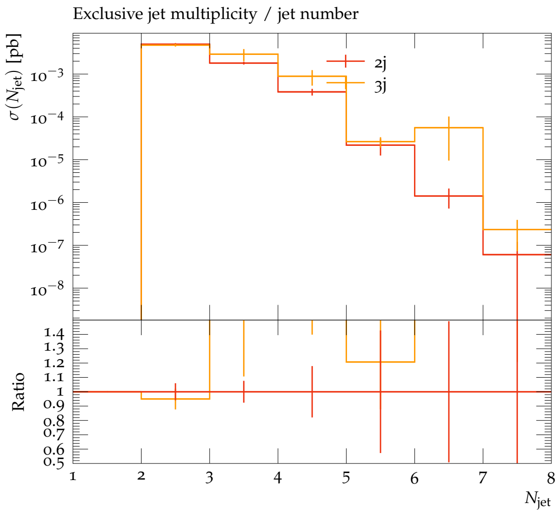

(b) strong background

Figure 6.3: Differential cross-section for the diphoton production at $\sqrt{s} = 13$ TeV in dependence of the number of jets from 100 million simulated events and with optimized cuts. Compared are the used simulation including up to 2 jets in the hard process and an advanced one including up to 3 jets.

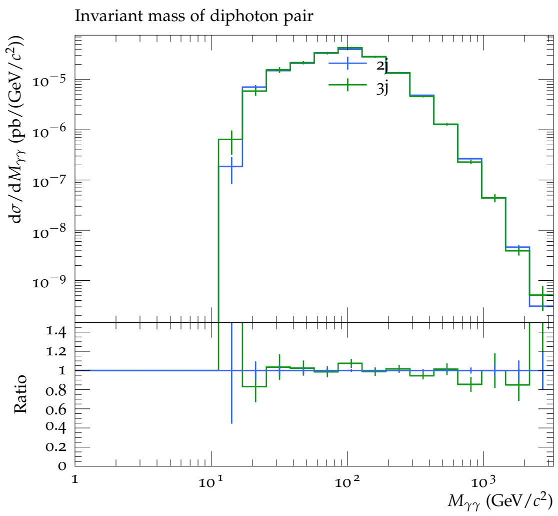

(a) electroweak signal

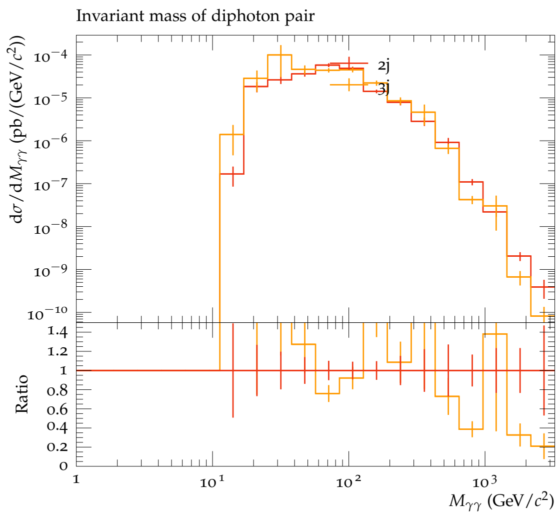

(b) strong background

Figure 6.4: Differential cross-section for the diphoton production at $\sqrt{s} = 13$ TeV in dependence of the diphoton invariant mass from 100 million simulated events and with optimized cuts. Compared are the used simulation including up to 2 jets in the hard process and an advanced one including up to 3 jets.

	σ_{QCD}/fb	σ_{EW}/fb	N_{QCD}	N_{EW}	Σ
2 jets simulated	7.2 ± 0.4	7.48 ± 0.05	1000 ± 50	1040 ± 7	32.9 ± 0.9
3 jets simulated	8.6 ± 1.1	7.56 ± 0.15	1200 ± 150	1051 ± 21	30.3 ± 2.0

Table 6.1: Cross-sections, expected event numbers at 139/fb and resulting observation significance of the electroweak diphoton production for the simulation up to 2 jets used throughout this thesis and a more advanced simulation including up to 3 jets in the hard process. The values originate from 100 million generated Monte Carlo events.

From all of this, it can be concluded that the two different simulations are compatible within their uncertainties. This means that the original 2 jet simulation and therefore the whole optimization is still valid. The plots also show that there is still an issue with the high statistic uncertainties of the background simulation, which again could only be resolved by investing more time and resources. But even with the advanced simulation the expected significance is still over 30 and will remain over 5 for systematic uncertainties of around 15%. The next step in advancing the simulations would be including next to leading order processes.

7 Summary and Outlook

The target of this thesis was to find out whether a measurement with the ATLAS Detector in LHC Run 2 could be sensitive to the electroweak diphoton plus jets production. The result, so far, is yes. The simulations performed for this thesis predict a significance of the electroweak signal over the background of $(32.9 \pm 0.9)\sigma$, which would certainly be enough to study the signal properly. This high sensitivity is a result of the analysis optimization done here and it even be improved by rerunning the steps of this optimization for different and more accurate simulations. However, the real measurement data will most likely not yield such high sensitivities since detector losses and the influence of systematic uncertainties have to be taken into account. The latter is also discussed throughout this thesis, which shows that even with a 20% additional systematic background uncertainty, a significant signal can still be expected. In general, this thesis contains mostly basic work and methods, which should be used as a basis to improve the sensitivity even further.

This leads to the outlook on the future perspectives on this subject, which are quite numerous. The most interesting usage of the simulated numbers and histogram would be a comparison to the actual measurement data from Run 2. This could then hint to the need for improved simulation, which is also briefly discussed in this thesis. Although the more advanced simulation here does not change the outcome greatly, it indicates the differences the simulations can make. Still to be tested are the corrections of the next to leading order processes or for example the results achieved with a different event generator. Also, the statistics of the background can still be improved by simply generating more event samples or the significance can be improved by multiple binning. These improvements might make a slight difference for the optimal analysis cuts, which would spark the need for the repetition of said optimization. All of this is only possible with a high effort in time and resources, which is why it was not done within this thesis, but it might very well be part of the future work on these processes.

In conclusion, this thesis shows that a very high sensitivity for the measurements of the electroweak diphoton production can be expected from the LHC Run 2 data and it presents multiple methods to optimize said sensitivity, which can be advanced and repeated in the future.

8 Bibliography

[1] Oliver Sim Brüning et al. *LHC Design Report*. CERN Yellow Reports: Monographs. Geneva: CERN, 2004. DOI: 10.5170/CERN-2004-003-V-1. URL: https://cds.cern.ch/record/782076.

[2] *LHC facts*. URL: https://home.cern/resources/faqs/facts-and-figures-about-lhc (visited on 06/09/2022).

[3] ATLAS Collaboration. *Luminosity determination in pp collisions at $\sqrt{s} = 13$ TeV using the ATLAS detector at the LHC*. Tech. rep. Geneva: CERN, June 2019. URL: https://cds.cern.ch/record/2677054.

[4] The ATLAS Collaboration et al. 'The ATLAS Experiment at the CERN Large Hadron Collider'. In: *Journal of Instrumentation* 3.08 (Aug. 2008), S08003–S08003. DOI: 10.1088/1748-0221/3/08/s08003. URL: https://doi.org/10.1088/1748-0221/3/08/s08003.

[5] T Gleisberg et al. 'Event generation with SHERPA 1.1'. In: *Journal of High Energy Physics* 2009.02 (Feb. 2009), pp. 007–007. DOI: 10.1088/1126-6708/2009/02/007. URL: https://doi.org/10.1088/1126-6708/2009/02/007.

[6] Enrico Bothmann et al. 'Event generation with Sherpa 2.2'. In: *SciPost Physics* 7.3 (Sept. 2019). DOI: 10.21468/scipostphys.7.3.034. URL: https://doi.org/10.21468%2Fscipostphys.7.3.034.

[7] Andy Buckley et al. 'LHAPDF6: parton density access in the LHC precision era'. In: *The European Physical Journal C* 75.3 (Mar. 2015). DOI: 10.1140/epjc/s10052-015-3318-8. URL: https://doi.org/10.1140%2Fepjc%2Fs10052-015-3318-8.

[8] Tanju Gleisberg and Stefan Höche. 'Comix, a new matrix element generator'. In: *Journal of High Energy Physics* 2008.12 (Dec. 2008), pp. 039–039. DOI: 10.1088/1126-6708/2008/12/039. URL: https://doi.org/10.1088/1126-6708/2008/12/039.

[9] Frank Krauss, Ralf Kuhn and Gerhard Soff. 'AMEGIC++ 1.0, A Matrix Element Generator In C++'. In: *Journal of High Energy Physics* 2002.02 (Feb. 2002), pp. 044–044. DOI: 10.1088/1126-6708/2002/02/044. URL: https://doi.org/10.1088%2F1126-6708%2F2002%2F02%2F044.

[10] Federico Buccioni et al. 'OpenLoops 2'. In: *The European Physical Journal C* 79.10 (Oct. 2019). DOI: 10.1140/epjc/s10052-019-7306-2. URL: https://doi.org/10.1140%2Fepjc%2Fs10052-019-7306-2.

[11] Matteo Cacciari, Gavin P. Salam and Gregory Soyez. 'FastJet user manual'. In: *The European Physical Journal C* 72.3 (Mar. 2012). DOI: 10.1140/epjc/s10052-012-1896-2. URL: https://doi.org/10.1140%2Fepjc%2Fs10052-012-1896-2.

[12] Matteo Cacciari, Gavin P Salam and Gregory Soyez. 'The anti-k_t jet clustering algorithm'. In: *Journal of High Energy Physics* 2008.04 (Apr. 2008), pp. 063–063. DOI: 10.1088/1126-6708/2008/04/063. URL: https://doi.org/10.1088/1126-6708/2008/04/063.

[13] *Rivet - MC analysis toolkit.* URL: https://rivet.hepforge.org/ (visited on 26/07/2022).

[14] *Analysis code for Rivet and ROOT.* URL: https://gitlab.mn.tu-dresden.de/flfo692b/Bachelor/ (visited on 05/09/2022).

[15] *Rivet analyses reference MC_DIPHOTON.* URL: https://rivet.hepforge.org/analyses/MC_DIPHOTON.html (visited on 26/07/2022).

[16] *Rivet analyses reference MC_PHOTONJETS.* URL: https://rivet.hepforge.org/analyses/MC_PHOTONJETS.html (visited on 26/07/2022).

[17] ATLAS Collaboration. *Photon identification in 2015 ATLAS data.* Tech. rep. Geneva: CERN, Aug. 2016. URL: https://cds.cern.ch/record/2203125.

[18] G. Aad, B. Abbott and D.C. Abbott et al. 'Differential cross-section measurements for the electroweak production of dijets in association with a Z boson in proton–proton collisions at ATLAS'. In: *The European Physics Journal C* 81.163 (2021). DOI: 10.1140/epjc/s10052-020-08734-w. URL: https://doi.org/10.1140/epjc/s10052-020-08734-w.

[19] *ROOT analysis framework.* URL: https://root.cern/ (visited on 19/08/2022).

[20] J. de Favereau et al. 'DELPHES 3: a modular framework for fast simulation of a generic collider experiment'. In: *Journal of High Energy Physics* 2014.2 (Feb. 2014). DOI: 10.1007/jhep02(2014)057. URL: https://doi.org/10.1007%2Fjhep02%282014%29057.

Erklärung

Hiermit erkläre ich, dass ich diese Arbeit im Rahmen der Betreuung am Institut für Kern- und Teilchenphysik ohne unzulässige Hilfe Dritter verfasst und alle Quellen als solche gekennzeichnet habe.

Florens Förster,
Dresden, 12 September 2022

9 Appendix

Run Card for SHERPA for the EW processes:

```
(run){
  % general setting
  EVENTS 100; ERROR 0.99;
  % scales, tags for scale variations
  FSF:=1.; RSF:=1.; QSF:=1.;
  SCALES STRICT_METS{FSF*MU_F2}{RSF*MU_R2}{QSF*MU_Q2};
  ALPHAQED_DEFAULT_SCALE=0.0

  % tags for process setup
  NJET:=0; LJET:=0; QCUT:=10;

  % me generator settings
  ME_SIGNAL_GENERATOR Comix Amegic LOOPGEN;
  OL_PREFIX=/projects/materie-09/sw-foss-2021b/OpenLoops/OpenLoops;
  LOOPGEN:=OpenLoops;
  EVENT_GENERATION_MODE Weighted;
  HEPMC_USE_NAMED_WEIGHTS=1;

  # EW corrections setup
  SCALE_VARIATIONS 0.25,0.25 0.25,1. 1.,0.25 1.,1. 1.,4. 4.,1. 4.,4.;
  PDF_VARIATIONS NNPDF30_nnlo_as_0118 NNPDF30_nnlo_as_0117 NNPDF30_nnlo_as_0119 MMHT2014nnlo68cl CT14nnlo PDF4LHC15_nnlo_30[all];
  ASSOCIATED_CONTRIBUTIONS_VARIATIONS=EW EW|LO1 EW|LO1|LO2 EW|LO1|LO2|LO3;
  METS_BBAR_MODE=5;

  # NWF improvements
  CSS_CSMODE = 1;
  PP_RS_SCALE VAR{0.25*sqr(PPerp(p[2])+PPerp(p[3]))};
  EXCLUSIVE_CLUSTER_MODE=1;
  CORE_SCALE=VAR{Abs2(p[2]+p[3])};

  % collider setup
  BEAM_1 2212; BEAM_ENERGY_1 = 6500.;
  BEAM_2 2212; BEAM_ENERGY_2 = 6500.;
  PSI_ItMin 25000;
  CDXS_VSOPT=5;
  Integration_Error 0.05;
  ANALYSIS Rivet;
}(run)

(processes){
  Process 93 93 -> 22 22 93 93 93{NJET};
  Order (0,4);
  Print_Graphs graphs;
  CKKW sqr(QCUT/E_CMS)/(1.0+sqr(QCUT/0.6)/Abs2(p[2]+p[3]));
  ME_Generator Amegic {LJET};
  RS_ME_Generator Comix {LJET};
  Loop_Generator LOOPGEN {LJET};
  Associated_Contributions EW|LO1|LO2|LO3 {LJET};
  End process;
}(processes)

(selector){
  "PT" 22 20,E_CMS:18,E_CMS [PT_UP]
  IsolationCut  22  0.1  2  0.10;
  DeltaR 22 22 0.2 1000.0;
  FastjetFinder antikt 2 20 0.0 0.4
}(selector)

(analysis){
  BEGIN_RIVET {
    -a FFBA_2022_1407 FFBA_2022_2508
  } END_RIVET
(analysis)
```

Run Card for SHERPA for the QCD processes:

```
(run){
  % general setting
  EVENTS 100; ERROR 0.99;

  % scales, tags for scale variations
  FSF:=1.; RSF:=1.; QSF:=1.;
  SCALES STRICT_METS{FSF*MU_F2}{RSF*MU_R2}{QSF*MU_Q2};

  ALPHAQED_DEFAULT_SCALE=0.0

  % tags for process setup
  NJET:=2; LJET:=0; QCUT:=10;

  % me generator settings
  ME_SIGNAL_GENERATOR Comix Amegic LOOPGEN;
  OL_PREFIX=/projects/materie-09/sw-foss-2021b/OpenLoops/OpenLoops;
  LOOPGEN:=OpenLoops;
  EVENT_GENERATION_MODE Weighted;
  HEPMC_USE_NAMED_WEIGHTS=1;

  # EW corrections setup
  SCALE_VARIATIONS 0.25,0.25 0.25,1. 1.,0.25 1.,1. 1.,4. 4.,1. 4.,4.;
  PDF_VARIATIONS NNPDF30_nnlo_as_0118 NNPDF30_nnlo_as_0117 NNPDF30_nnlo_as_0119 MMHT2014nnlo68cl CT14nnlo PDF4LHC15_nnlo_30[all];
  ASSOCIATED_CONTRIBUTIONS_VARIATIONS=EW EW|LO1 EW|LO1|LO2 EW|LO1|LO2|LO3;
  METS_BBAR_MODE=5;

  # NWF improvements
  PP_RS_SCALE VAR{0.25*sqr(PPerp(p[2])+PPerp(p[3]))};
  EXCLUSIVE_CLUSTER_MODE=1
  CORE_SCALE=VAR{Abs2(p[2]+p[3])};

  % collider setup
  BEAM_1 2212; BEAM_ENERGY_1 = 6500.;
  BEAM_2 2212; BEAM_ENERGY_2 = 6500.;

  PSI_ItMin 25000;
  CDXS_VSOPT=5;
  Integration_Error 0.05;

  ANALYSIS Rivet;
}(run)

(processes){
  Process 93 93 -> 22 22 93{NJET};
  Order (*,2);
  Enhance_Factor 100 {4};
  Print_Graphs graphs;
  CKKW sqr(QCUT/E_CMS)/(1.0+sqr(QCUT/0.6)/Abs2(p[2]+p[3]));
  ME_Generator Amegic {LJET};
  RS_ME_Generator Comix {LJET};
  Loop_Generator LOOPGEN {LJET};
  Associated_Contributions EW|LO1|LO2|LO3 {LJET};
  End process;
}(processes)

(selector){
  "PT" 22 20,E_CMS:18,E_CMS [PT_UP]
  IsolationCut  22  0.1  2  0.10;
  DeltaR 22 22 0.2 1000.0;
}(selector)

(analysis){
  BEGIN_RIVET {
    -a FFBA_2022_1407 FFBA_2022_2508
  } END_RIVET
(analysis)
```